



# Experimental study on seismic performance of ultrahigh-strength steel frames with buckling-restrained braces

Sheng Pei<sup>1,2</sup> · Zhe Zhang<sup>1</sup> · En-Feng Deng<sup>1</sup> · Yan-Bo Wang<sup>3</sup>

Received: 1 June 2021 / Revised: 11 September 2021 / Accepted: 24 September 2021 / Published online: 10 October 2021  
© Wrocław University of Science and Technology 2021

## Abstract

The application of high-strength steel (HSS) is a significant trend in the development of steel structures. Two main challenges for HSS structures in seismic design (i.e., low energy dissipation capacity and low lateral stiffness) need to be addressed before HSS structures can be widely constructed in practice. To solve those problems, the seismic performance of structures combined of HSS frames and concentric buckling-restrained braces (BRBs) was investigated in this study. Two half-scale experimental specimens with different stiffness ratios between BRB and HSS frame were fabricated and tested under constant vertical load and cyclic increasing horizontal load. The hysteretic response, horizontal bearing capacity, internal force distribution, energy dissipation capacity, and ductility of the dual system were analyzed. The results showed that the specimens exhibited overall ductile performance with high elastic stiffness, significant ductility, and excellent energy dissipation capacity. The characteristics of both specimens in the pseudo-static test can be divided into three typical phases, which were described as overall elastic phase, BRB hardening phase, and failing phase. The BRB hardening phase was characterized by high energy dissipation capacity, and the plastic deformation was limited to the BRB, so the ductile demand of HSS member in HSSF-BRB was reduced. Moreover, the effect of stiffness ratio between BRB and HSS frame on seismic performance was discussed in this paper.

**Keywords** High-strength steel · Dual system · Cyclic test · Seismic performance · Buckling-restrained brace

## 1 Introduction

With recent advancements in metallurgy technology and welding techniques, the use of high-strength steel (HSS, steel having nominal yield strength not lower than 460 MPa) and ultrahigh-strength steel (UHSS, HSS having nominal yield strength not lower than 690 MPa) in structural engineering is increasing rapidly [1]. Compared with normal steel with low yield strength, HSS structures are characterized by better economic [2], environmental and mechanical benefit [3]. Galambos et al. [4] highlighted the advantages of HSS, which include light weight, small cross-section and

high elastic strength. Collin [5] notes that even though the price of structural steel increase with the steel grade, the overall construction costs of HSS structures is reduced owing to savings in material and fabrication costs.

Nevertheless, there are challenges in the seismic application of HSS structures that need to be addressed before those structures can be widely constructed in practice. Current methods used for evaluating the seismic response of steel structures are basically based on the dissipative design philosophy [6]. Accordingly, the materials of steel structures are expected to deform plastically when subjected to strong earthquakes for the purpose of dissipating seismic energy and reducing seismic response. Consequently, codes for seismic design of steel structures around the world impose limits on the plasticity of structural steel (e.g., elongation and strength ratio). Typically, HSS members, connections and frames exhibit poor ductility and low energy dissipation capacity due to limited processing process [7], and have a higher risk of brittle fracture and hydrogen-induced cracking when the material turns into plastic [8]. Hence, the application of HSS structures in seismic region is restricted [9]

✉ En-Feng Deng  
dengenfeng@zzu.edu.cn

<sup>1</sup> School of Civil Engineering, Zhengzhou University, Henan Province, Zhengzhou 450001, China

<sup>2</sup> School of Civil Engineering, Henan University of Engineering, Henan Province, Xinzheng 451191, China

<sup>3</sup> School of Civil Engineering, Tongji University, Shanghai 200092, China

Another challenge associated with HSS structures in seismic design comes from the reduced lateral stiffness, which is accompanied by the reduction of the column sections [10]. Tenchini et al. [11] showed that the benefit of using HSS in moment resisting frames for seismic application is limited, because the design of moment resisting frames is conditioned to satisfy the performance limit in terms of story drift ratio. Hoang et al. [12] reported that the use of HSS in braced frames could enhance the advantage of HSS, particularly for columns, because strength criteria determine the design of braced structure. Moreover, Andre et al. [13] found that the braced frame is characterized by a significant brace-ductility demand.

Recently, the concept of “damage-free structures” has aroused more and more attention in the seismic design of HSS structures [14]. This design concept involves dual systems combined of HSS components and ductile members. HSS are utilized for non-dissipative members that designed to deform elastically, and inelastic deformation is restricted to ductile and energy-dissipating members. Thus, the dual systems could induce an overall ductile mechanism in earthquakes for energy dissipation without plastic deformation in the HSS members. Recent studies [15] have shown the advantages of those dual systems in the overall ductile mechanism for controlling the seismic response of multistory buildings and decreasing the ductile demand of HSS members. Moreover, compared to common steel frame, HSSF has larger yield drift ratio and lower lateral stiffness, both of which are favorable to maximize combined effect of BRB frames.

The structure combined of HSS frames and buckling-restrained braces (HSSF-BRB) was developed and studied in this paper. Buckling-restrained braces (BRBs) have similar tensile and compressive capacities in preventing buckling under compressive forces, which are widely used in new and existing buildings sited in the seismic regions [16]. The BRBs in the dual system of HSSF-BRB can provide enhanced lateral stiffness, strength and energy dissipation capacity. Furthermore, the strength and stiffness of BRB can be adjusted by specifying appropriate yield strength and geometric properties. Therefore, the “damage-free structure” concept for HSSF-BRB can be easily implemented by the applying capacity-design criteria.

This study is focused on the seismic performance of the dual system of HSSF-BRB. The enhanced strength, stiffness and energy dissipation capacity of HSSF-BRB may enhance the seismic application of HSS in construction engineering [17]. Pseudo-static tests were performed on two half-scaled specimens, each comprising a HSS frame and a BRB. The primary objective of the test was to evaluate the performance of HSSF-BRBs with different stiffness ratios between BRB and frame. The following sections in

this paper describe the specimen details, test setup, experimental observations, and test results.

## 2 Experimental program

### 2.1 Details of test specimens

Two half-scale specimens, denoted as SP-1 and SP-2, were designed, constructed and tested. Each specimen consisted of a 1-story single-span HSS moment frame and a single diagonal BRB. The HSS frame in both specimens was extracted from the first floor of a half-scaled 12-story prototype planar frame, as shown in Fig. 1, which was designed according to the Chinese design code for steel structures (GB50017-2017) [18]. A dead load of  $6 \text{ kN/m}^2$  and a live load of  $2 \text{ kN/m}^2$  were applied to the floors and roof, and a wind load having a basic wind pressure of  $0.5 \text{ kN/m}^2$  was applied as the lateral load.

The details of the HSS steel frame in both specimens are shown in Fig. 2. Beams and columns were made of welded wide-flange steel members. Q690 UHSS (nominal yield strength: 690 MPa) and Q345 normal steel (nominal yield strength: 345 MPa) were adopted for the columns and beams, respectively, to maximize structural efficiency [13]. The beam-to-column connections were directly welded together to form moment-resisting connections. The cross-section classification for beams and columns are both noncompact. In addition, vertical stiffeners were fillet-welded to the column flange and base plate in each column to strengthen the welds in the column base. Similarly, the segments of the beam-to-column connections and brace-to-frame connections were strengthened using full-depth stiffeners to prevent the premature local buckling of the webs. The welds in the specimen were designed to have higher strength than the

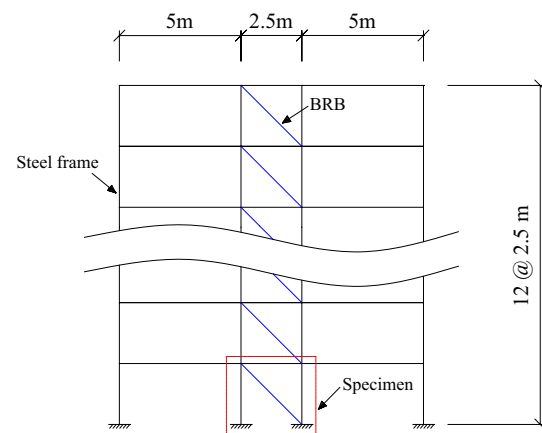


Fig. 1 Prototype frame

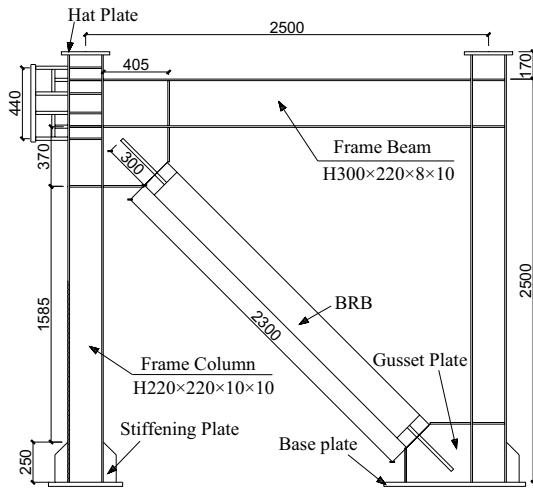
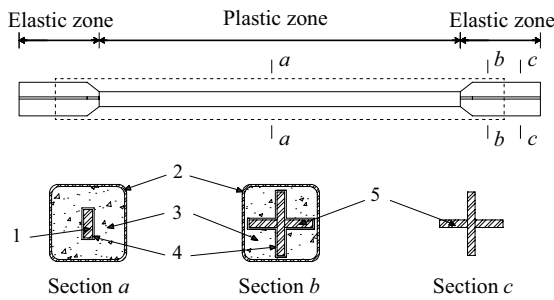


Fig. 2 Details of the specimens (mm)



1 = Plastic zone, 2 = Steel hollow, 3 = Concrete, 4 = Isolation material, 5 = Elastic zone (1 and 5 are core region, 2 and 3 are casing member)

Fig. 3 Components of BRB

yield strength of the welded steel plate, so the welds were expected not to fail before the steel plate yields.

A BRB was concentrically connected to each steel frame at the beam-to-column connections using gusset plates through welding. The thicknesses of gusset plates were 14 and 20 mm for SP-1 and for SP-2, respectively. The stability and strength of the gusset plates were evaluated following the specification of the Chinese design code for steel structures (GB-50017–2017) [18]. Both BRBs that attached to the specimens consisted of the core region, the casing member, and the isolation material (Fig. 3). Steel hollows were utilized as casing members to restrain the buckling of the core region and prevent the overall buckling of the BRB, as shown in Fig. 4. The core region was composed of plastic zone and the elastic zone, as shown in Fig. 5. The plastic zone was designed to provide stiffness and strength, and yield first to dissipate seismic energy. The elastic zone was designed to provide a connection between the plastic zone and gusset plate and remain elastic at the maximum forces that the brace can develop. Moreover, the core

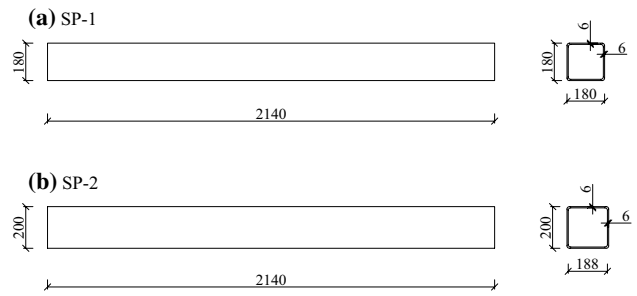


Fig. 4 Details of steel hollows (mm)

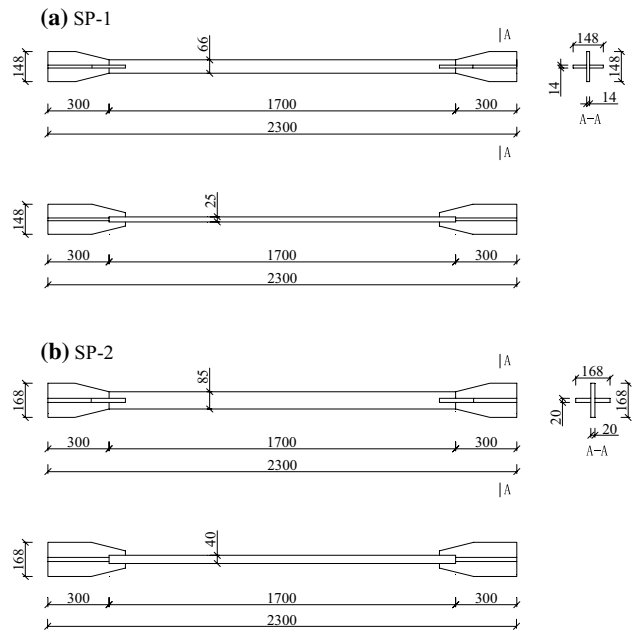


Fig. 5 Details of core regions (mm)

region and casing member were separated by the isolation material. The cross-sections of the plastic zone of the core region, elastic zone of the core region, and steel hollow of the casing member were rectangular, regular cruciform, and square tubular, respectively. The proportion of the BRB was controlled based on the brace-to-frame stiffness ratio,  $\tau$  ( $\tau = K_b/K_f$ , where  $K_b$  represents the horizontal stiffness of the brace,  $K_f$  represents the horizontal stiffness of the steel frame), which was 2 for SP-1 and 4 for SP-2. The theoretical value of the axial yield strength of the BRB (denoted as  $F_{ya}$ ,  $F_{ya} = f_y \times A_p$ , where  $f_y$  and  $A_p$  are the yield strength and section area of the plastic zone, respectively), which were 500 kN for SP-1 and 1000 kN for SP-2.

It should be note that in actual applications, the installation of BRBs is only allowed after the main structure is constructed to minimize the contribution of the BRB to the vertical force. However, owing to the limitation of the test

**Table 1** Material properties of specimens

Section	Steel	t (mm)	$f_y$ (MPa)	$f_u$ (MPa)	A(%)	Y/T
Frame beams	Q345	10	417	554	29	0.75
	Q345	8	408	538	28	0.76
Frame columns	Q690	10	797	839	17	0.95
Plastic zone of BRB for SP-1	Q235	20	308	455	31	0.68
Plastic zone of BRB for SP-2	Q235	40	298	470	31	0.63

$t$ ,  $f_y$ ,  $f_u$ ,  $A$ , and  $Y/T$  are the thickness, yield strength, ultimate strength, elongation and yield ratio, respectively

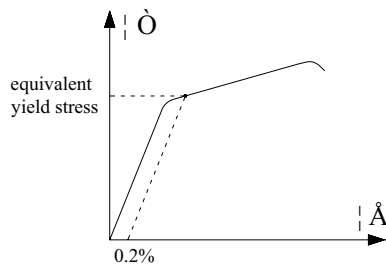


**Fig. 6** Stress–strain curve and equivalent yield stress for Q690 steel

conditions, the installation of the BRB in the specimen was completed before the axial force was applied to the column.

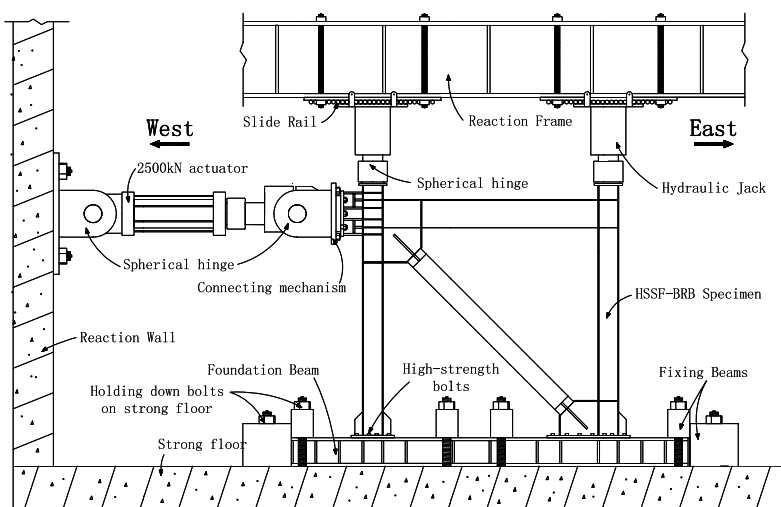
### 2.2 Material properties

The material properties of the steel plates were determined through coupon tensile tests [19] except for those that were designed to remain elastic. Three identical specimens for each type of steel plates were tested, and the average values were obtained as the actual material properties, as shown

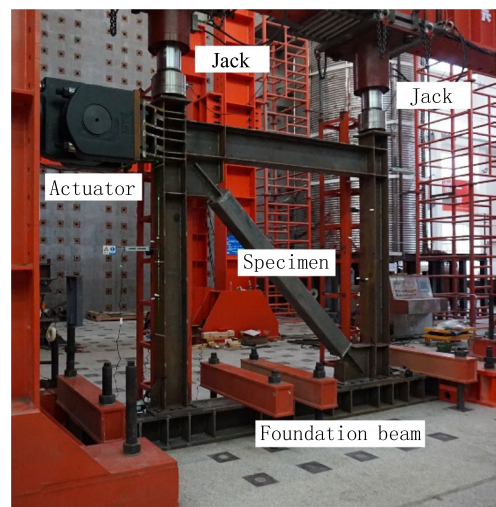
in Table. 1. It should be noted that the tensile stress–strain curves for Q690 steel did not exhibit a noticeable yield point. Thus, the proof stress corresponding to 0.2% residual plastic strain was adopted as the equivalent yield stress, as shown in \\* MERGEFORMAT Fig. 6. It can be inferred that with the increase of steel strength, the elongation decreased and the yield ratio increased. The elongation and yield ratio of Q690 steel were 17% and 0.95, respectively, which exceeded the limits for structural steels according to the Chinese code for seismic design of buildings (GB50011-2010) [20].

### 2.3 Test setup

The overview of the test setup is shown in Fig. 7. A 2500 kN servo-actuator with  $\pm 350$  mm stroke length was employed to apply low-cyclic horizontal load at beam level. The servo-actuator was directly connected to the specimen using high-strength bolts. Two spherical-headed hydraulic jacks with 2000 kN loading capacity were used to exert axial forces on each column. The hydraulic jacks were fixed to a slid rail, which was in turn fastened to the reaction frame, so the jacks could move horizontally along with the top end of



**(a)** Schematic diagram



**(b)** On site photo

**Fig. 7** Test setup

columns. A rectangular base plate of 25 mm thickness were welded to each bottom end of columns, which were in turn, connected to the fundamental beam using M24 high-strength bolts. The fundamental beam was firmly fixed to the strong floor by fixing beams and holding down bolts. Accordingly, the boundary conditions of the column bases were considered to be rigid.

### 2.4 Loading program

Constant vertical loads and cyclic horizontal loads were applied to the specimens during test process. First, a constant axial load of 1100 kN (corresponding to 25% of the nominal yield strength of the column) was applied on the hat

plate of each column using hydraulic jacks to simulate the gravity load of the upper stories. Next, hysteretic horizontal loads were applied based on the prescribed displacement loading protocol. The displacement protocol recommended in the American Institute of Steel Construction (AISC) seismic provisions [21] was adopted with slight modifications (Fig. 8). Inter-story drift ratios were increased from 0.125 to 3% and applied as the target amplitudes, and several complete loading cycles were included in each amplitude. The early amplitude of 0.125% and 0.25% were applied to detect any detrimental effects before the plastic behavior of the BRB was reached, which were not recommended in the AISC provisions. Because a drift ratio of 2% corresponded to inelastic drift limits for steel frames based on the Chinese seismic code, an amplitude of 3% drift ratio was applied to evaluate the ultimate state of the specimen. The positive and negative directions in the loading program (Fig. 8) corresponded to the east and west directions in Fig. 7, respectively.

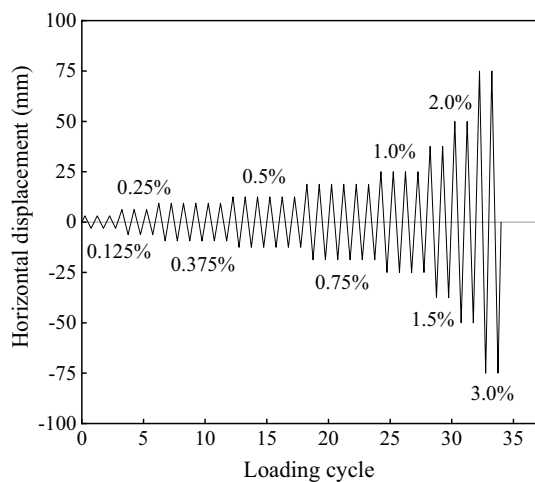


Fig. 8 Loading protocol

### 2.5 Instrumentation

Each specimen was instrumented with displacement transducers, strain gauges, right-angled strain rosettes, and load cells, as shown in Fig. 9. A load cell was attached to the head of each actuator (LC1) and jack (LC2 and LC3) to measure the applied horizontal and vertical loads. Four strain gauges (SGa to SGd) were attached to the edges of the flanges in each cross-section from S1 to S8. Three strain rosettes were attached to both column webs at mid-height level (SR1 and SR2) and the eastern panel zone of steel frame (SR3), respectively. Moreover, displacement transducers with

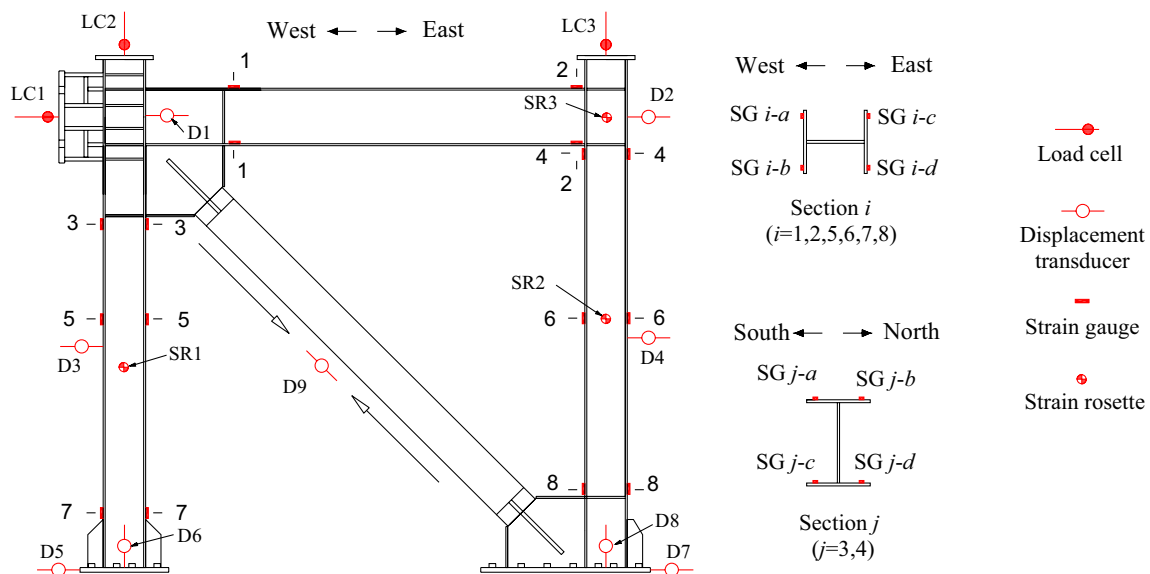


Fig. 9 Schematic diagram of instrumentation

various gauge lengths were used to measure the horizontal displacement at the beam level (D1 and D2), the horizontal displacement at mid-height level (D3 and D4) and the axial deformation of the BRB (D9). The movements of both column base plates were also monitored horizontally (D5 and D7) and vertically (D6 and D8).

### 3 Experimental observation and failure modes

#### 3.1 Specimen SP-1

During the early-loading stages of SP-1 (i.e., the drift ratio from 0.125 to 1%), no significant experimental phenomenon was observed, and the HSS steel frame essentially remained elastic. As the horizontal displacement continued to increase, visible in-plane flexural deformation occurred in the ends of the columns and beams. At the drift ratio of 2%, the flexural deformation became rather remarkable near column bases and beam-column connections, which indicated that plastic deformation developed in these regions. In the first half-cycle with 3% drift ratio (i.e. actuator loaded to the east), local buckling occurred at the outer flange near the east column base just beyond the edge of gusset plate (Fig. 10a). In the following half-cycle with 3% drift ratio (i.e. actuator loaded to the west), local buckling occurred in the outer flange near the bottom of the west column (Fig. 10b) and the inner flange at the top of the west column (Fig. 10c). In the second cycle of the 3% loading stage, the local buckling mentioned above developed further. No visible cracks or fractures were formed on any of the steel plates or welds of SP-1.

#### 3.2 Specimen SP-2

The observations of specimen SP-2 were quite similar to those of SP-1. During the early loading stages with inter-story drift

ratio from 0.125 to 1.5%, rotations at the ends of the columns and beam increased without local buckling or cracking. With the inter-story drift continued to increase, local buckling initially occurred in the outer flange near the west column base (Fig. 11a) during the second half-cycle (i.e. actuator loaded to the west) with 2% drift ratio. During the first half-cycle (i.e. actuator loaded to the east) with 3% drift ratio, significant local buckling occurred in the outer flange near the base of east column just beyond the edge of gusset plate (Fig. 11b). A partial fracture was also initiated during this half-cycle between the outer flange of west column and the base plate. In the second half-cycle (i.e. actuator loaded to the west) with 3% drift ratio, local buckling occurred in the inner flange at the top of the west column (Fig. 11c). During the third half-cycle with 3% drift ratio, the partial fracture at the base of west column

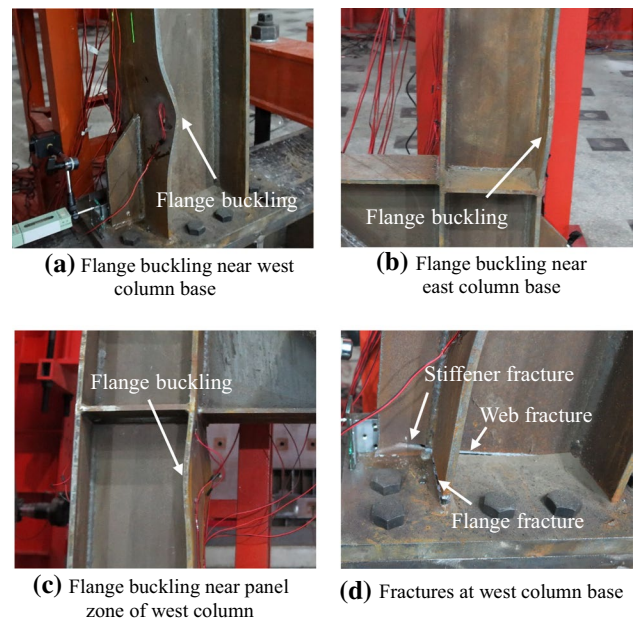


Fig. 11 Failure mode of SP-2 during test

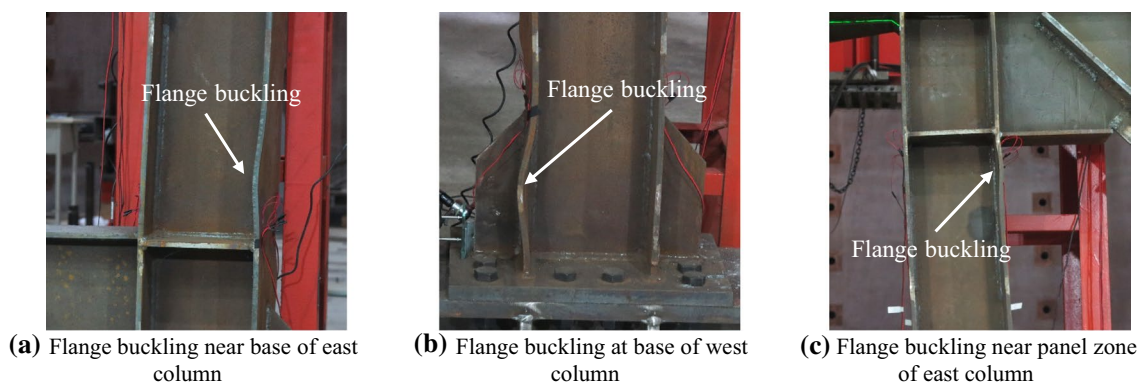


Fig. 10 Failure mode of SP-1 during test

expanded to the complete flange fracture and developed to the web and stiffener (Fig. 11d).

Furthermore, a significant relative slip between the core region and casing member was observed in both positive and negative directions (Fig. 12), which indicated stable plastic deformation capacity of the core region and demonstrated the effectiveness of the BRB. It should be mentioned that Fig. 11 only show the observation for SP-2, similar phenomenon could be observed for SP-1.

### 4 Test results and discussion

#### 4.1 Horizontal load–displacement responses

According to classical mechanics theories, shear strains are uniformly distributed in the web section when wide flange members are subjected to shear force. Therefore, the horizontal force in each steel frame ( $F_{frame}$ ) of the specimens could be obtained based on the strain measurements of SR1 and SR2 (Fig. 9) by the following equations:

$$F_{frame} = \sum \frac{\sigma_1 - \sigma_2}{2} \sin(2\varphi_0) A_{web}, \tag{1}$$

$$\sigma_1 = \frac{E}{1 - \nu} A + \frac{E}{1 + \nu} \sqrt{B^2 + C^2}, \tag{2}$$

$$\sigma_2 = \frac{E}{1 - \nu} A - \frac{E}{1 + \nu} \sqrt{B^2 + C^2}, \tag{3}$$

$$\varphi_0 = \frac{1}{2} \arctan \frac{B}{C}, \tag{4}$$

where  $A_{web}$  is the section area of the column web;  $\sigma_1$  and  $\sigma_2$  are the principal stresses in the column web;  $\varphi_0$  is the orientation angle of the principal stress in the column web;  $\nu$  is Poisson’s ratio of steel, which was determined as 0.3;  $E$  is Young’s modulus that is equal to 206 GPa. The parameters  $A$ ,  $B$ , and  $C$  are related to the strain rosette type and were calculated using the following equations:  $A = (\epsilon_0 + \epsilon_{90})/2$ ,  $B = (\epsilon_0 - \epsilon_{90})/2$ , and  $C = (2\epsilon_{45} - \epsilon_0 - \epsilon_{90})/2$ ;  $\epsilon_0$ ,  $\epsilon_{45}$  and  $\epsilon_{90}$  are the strain quantities along  $0^\circ$ ,  $45^\circ$ , and  $90^\circ$  directions, respectively.

Because it was difficult to directly measure the strain of the core segment of BRB when loading, the horizontal force of the BRB ( $F_{BRB}$ ) was obtained based on the equilibrium of the horizontal force using the following expression,  $F_{BRB} = F - F_{frame}$ , where  $F$  represents the inter-story shear.

Hysteresis curves and skeleton curves of the horizontal force versus the inter-story drift were plotted for overall structures (Fig. 13), steel frames (Fig. 14) and BRBs (Fig. 15). The inter-story drift in the vertical axis corresponded to the actual displacement measured by D1 (see Fig. 9), which was slightly less than the value that required by the loading protocol, particularly in the negative direction, primarily due to the unfavorable deformation of the connecting bolts between the specimen and actuator. The skeleton curves were constructed from the hysteresis curves by sequentially connecting the end points of each loading amplitude for the first loop.

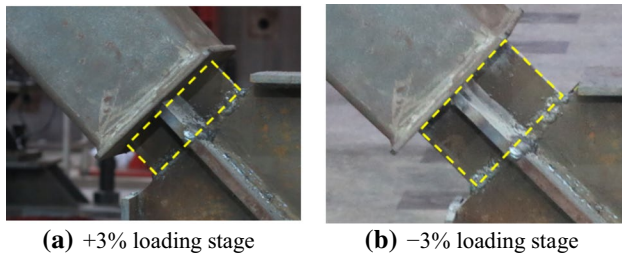


Fig. 12 Relative slip between casing member and core region

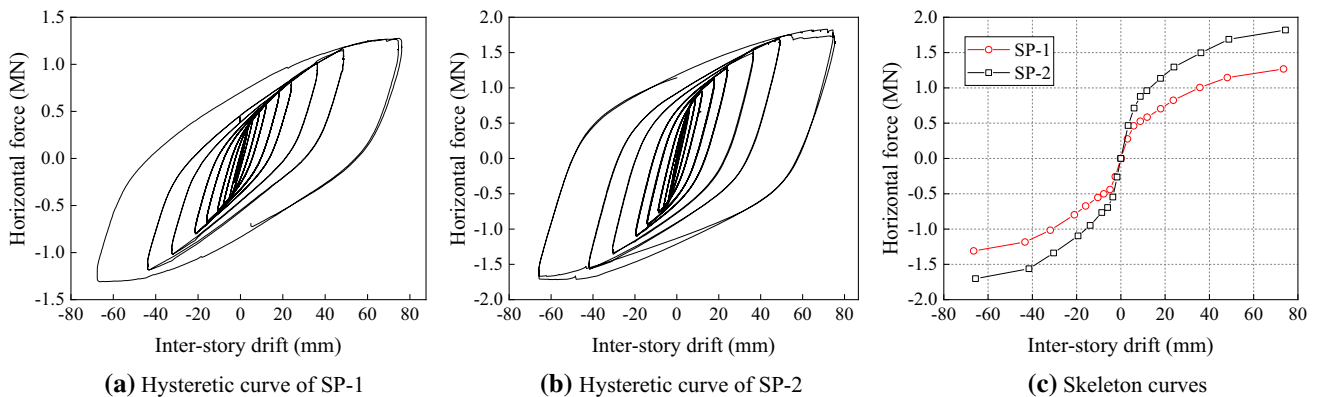


Fig. 13 Load–displacement curves of the specimens

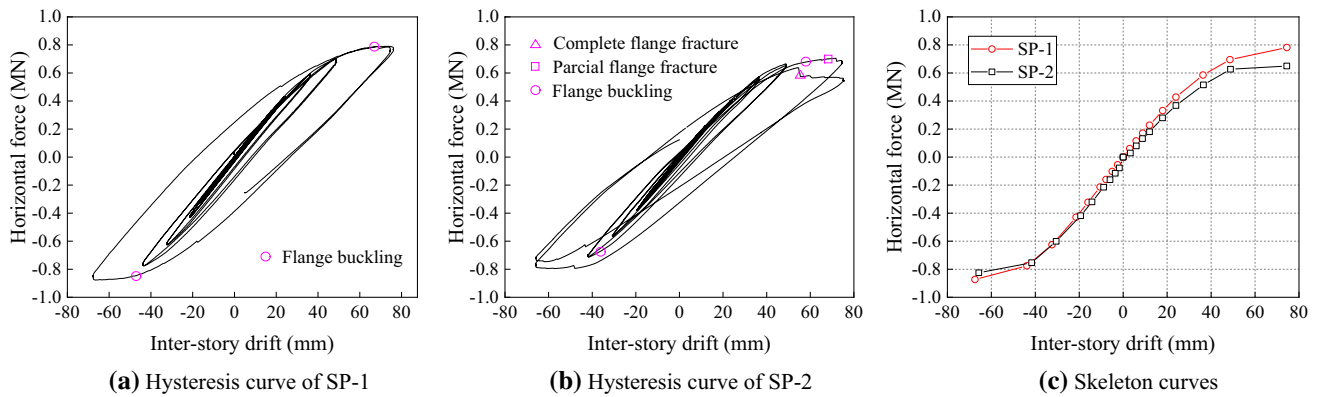


Fig. 14 Load–displacement curves of the frames

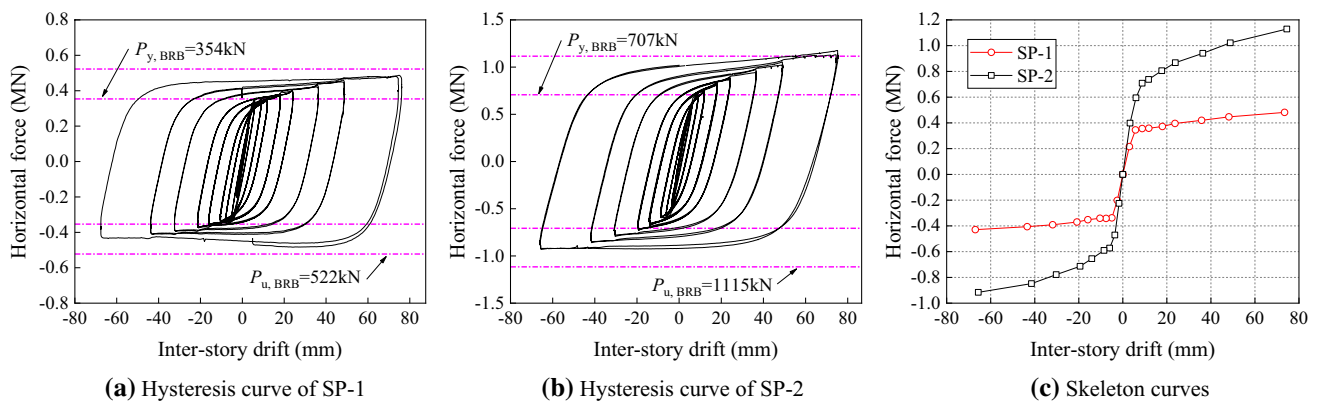


Fig. 15 Load–displacement curves of the BRBs

Figure 13 shows the hysteresis curves and skeleton curves of the overall structures. It was found that the specimens enforced an overall ductile mechanism, and exhibited a nearly bilinear elastic–plastic hysteretic response before severe buckling occurred in the column bases. The hysteretic curves of the specimens were stable and full. The stiffness (i.e. slope of the curves) decreased significantly after the BRB yield. The lateral stiffness and energy dissipation capacity increased significantly with the stiffness ratio between BRB and HSS frame.

Figure 14 shows the hysteresis and skeleton curves of the HSS frame. The onset of the critical observations of HSS frame, such as flange buckling, partial flange fracture and complete flange fracture, was marked in the corresponding hysteresis curves. It is found that the HSS frame exhibited a large flexible deformation capacity, which were favorable for combined effect between BRB and steel frame. Although the plastic deformation could be found beyond the 1% loading stage (as identified through stiffness degradation), the permanent drift of the HSS frame (which corresponds to distance from the intersection of hysteretic curve and transverse

axis to the origin) did not significantly increase before local buckling occurred in column bases. Similar hysteretic responses were found for both HSS frames in elastic stage, and in plastic stage, the frame stiffness degrade faster with the increase of BRB stiffness. For SP-2, a crack developed in the west column base owing to high level of tensile stress, resulting in a sudden strength degradation in the second half with 3% drift ratio.

Figure 15 shows the hysteresis and skeleton curves of the BRBs. The hysteretic response of the BRBs showed significant bilinear elastic–plasticity property, and characterized as low yield displacement and stable hardening capacity. The theoretical yield force ( $F_{y, BRB}$ ) and ultimate force ( $F_{u, BRB}$ ) of BRB were plotted in the figure for comparison.  $F_{y, BRB}$  and  $F_{u, BRB}$  were calculated based on the actual geometry and material properties of the BRB core by  $F_{y, BRB} = A_p \sigma_y \cos \theta$  and  $F_{u, BRB} = A_p f_u \cos \theta$ , where  $A_p, f_y, f_u$  and  $\theta$  represent the sectional area of plastic zone, yield stress of plastic zone, ultimate stress of plastic zone and inclination angle of BRB, respectively. The ratio between the actual and theoretical yield force were 1.01 and 0.96 for SP-1 and SP-2,



respectively, which verified the reliability of the hysteretic curves.

Figure 16 shows the horizontal force of the HSS frame and BRB. As shown, the story shear was share by BRB and steel frame. The BRB in each specimen enhanced the strength of the structure, especially at low displacement levels where BRB carried most of the story shear. The enhanced strength of the structures with low story-drift could facilitates flexible seismic design under frequent earthquakes.

Based on the test results and hysteresis curves, the typical characteristics of the HSSF-BRB specimens in pseudo-static tests can be summarized in three phases, which were described as overall elastic phase, BRB hardening phase, and failing phase, as shown in Fig. 17. For overall elastic phase (i.e., OA in Fig. 17), both the BRB and HSS frame remained in the elastic range. The performance of HSSF-BRB in this phase can be summarized as high lateral stiffness and low permanent drift. For BRB hardening phase (i.e., AB in Fig. 17), the BRB yielded at the beginning of the phase, and the HSS frame essentially remained in the elastic state. The performance of HSSF-BRB in this phase can be summarized as overall ductile deformation, stable hardening capacity and excellent energy dissipation capacity. For failing phase (i.e., BC in Fig. 17), plastic deformation developed in the steel frame with local buckling and fracture. This phase is not recommended for seismic design of HSSF-BRB due to high risk of non-ductile destruction.

### 4.2 Internal force distribution

The normal strains in the column flanges combined with the flexural strains (i.e., strains owing to bending moment) and axial strains (i.e., strains owing to axial force). The bending moment in each column section (i.e. S3–S8 in Fig. 9) was calculated according to the strain measurement in the flanges of the corresponding section. Based on the sectional distribution rule of flexural and axial strains, the following

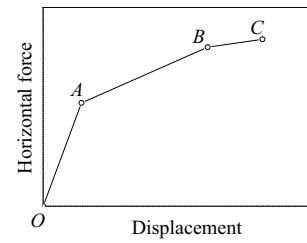


Fig. 17 Force mechanism

theoretical formula was used to calculate bending moment ( $M$ ) in each section:

$$M = \frac{EI_x(\epsilon_1 - \epsilon_2)}{d_c}, \tag{5}$$

where  $\epsilon_1$  and  $\epsilon_2$  are the average normal strains in the west and east flanges of the columns, respectively, and  $I_x$  is the second moment of area about the main axis.

The axial force in the column was considered to remain constant within the column length. Therefore, the axial column force was determined according to the strain quantities in column flanges measured at the mid-span section (i.e., S5 and S6 in Fig. 9) by:

$$F = \frac{EA_{col}(\epsilon_1 + \epsilon_2)}{2}, \tag{6}$$

where  $A_{col}$  is the sectional area of the column.

The moment distributions in the columns at various loading stages are depicted in Fig. 18. The position of each section in the horizontal axis was in proportion to the actual position of each section in the columns. It was found that the calculated results of bending moment in column ends became unreliable when the drift ratio exceeded 1% due to inelastic strain. Therefore, the loading stages in Fig. 18 was limited to the loading stages from  $-1$  to  $1\%$ , where the framing members essentially remained within

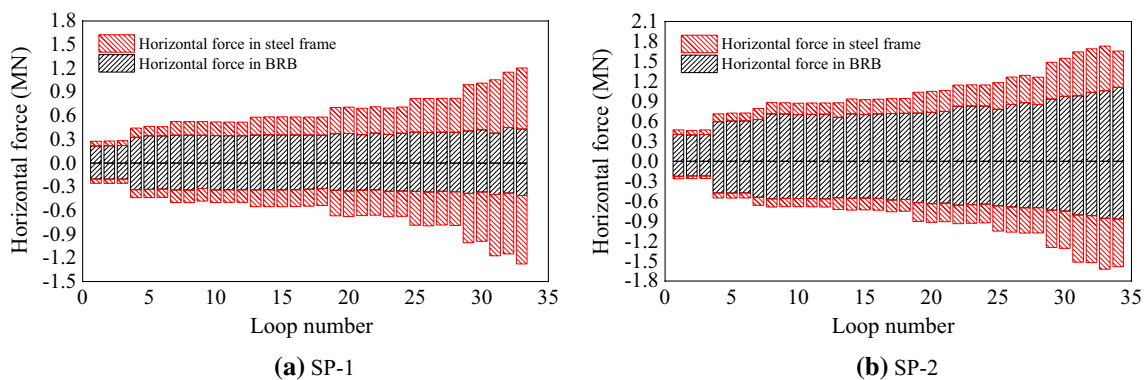
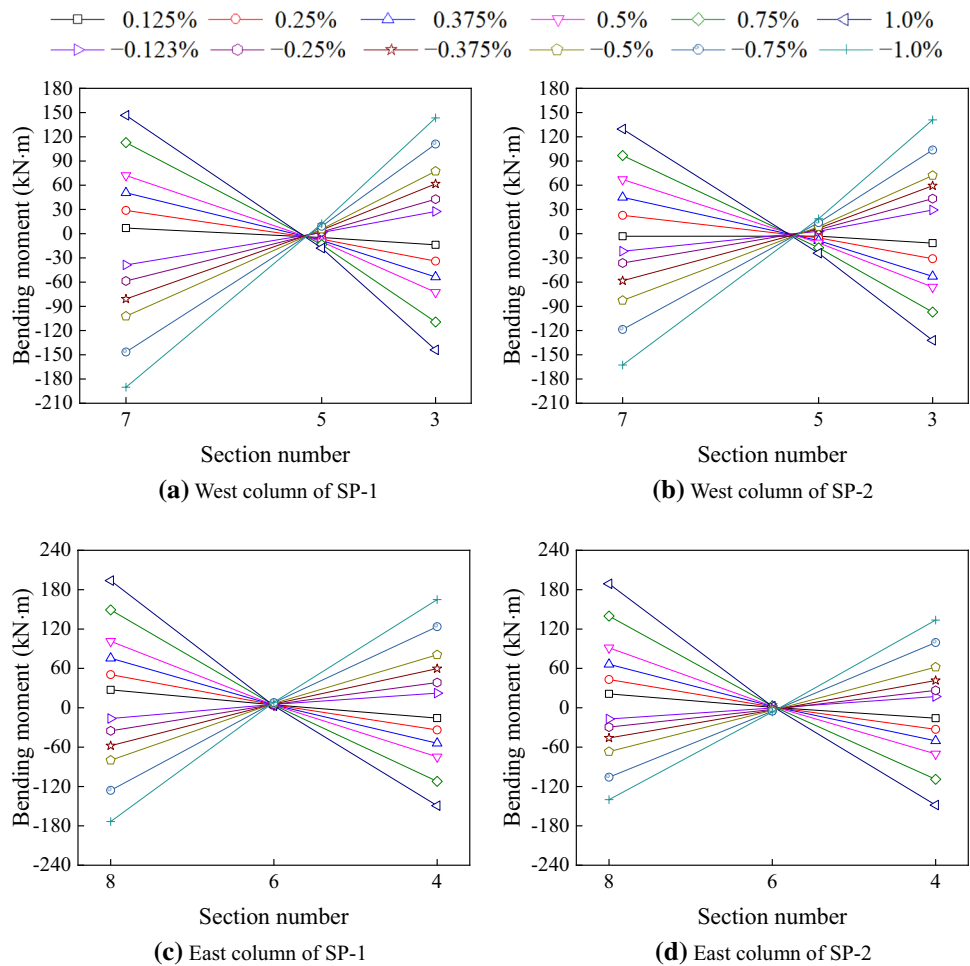


Fig. 16 Horizontal force of HSS frame and BRB

**Fig. 18** Moment distribution in the columns

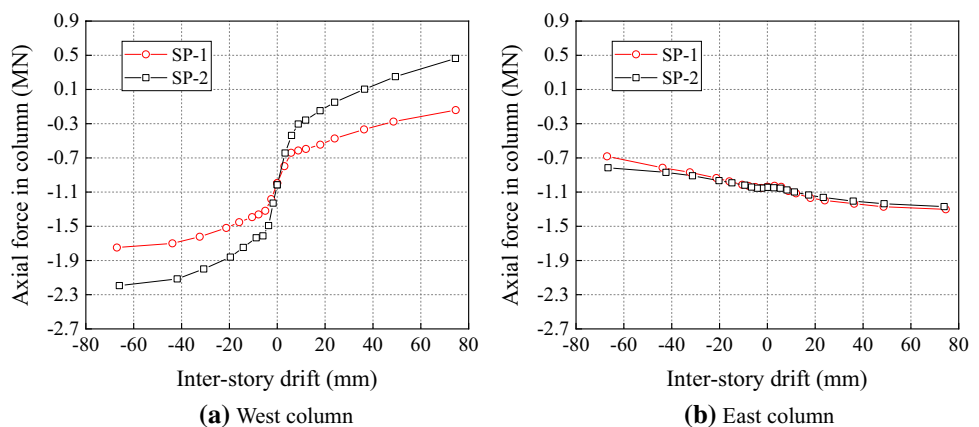


the elastic range. For both specimens, the bending moment in the column varied almost linearly along the column length. The maximum moment appeared at both ends of the column, and the moment typically increased proportionally with the horizontal deformation. The inflection point remained unchanged with various loading amplitudes. A comparison between the two specimens showed

that the effect of  $\tau$  on the column bending distribution was minimal.

The curves of the column axial force versus the horizontal displacement are plotted in Fig. 19. The actual initial axial forces in the west column of SP-1, the west column of SP-2, the east column of SP-1, and east column of SP-2 were 996 kN, 1015 kN, 1039 kN, and 1044 kN, respectively. These

**Fig. 19** Axial forces in columns



values were slightly lower than the load (1100kN) applied on the hat plate of each column, owing to the unfavorable contribution of the BRB to the vertical load, as described previously. For the west columns in both specimens (Fig. 19a), with the increase of horizontal displacement, the axial forces varied in proportion to the component shear of the BRB, and the variation is larger with higher BRB stiffness. Tensile axial force appeared in the west column of SP-2 with large positive displacement. The variation of the axial force in the east column was relatively gentle. (Fig. 19b). Given that the vertical load on the column top was monitored and kept constant during the test, the most possible source of the axial force variation in east column was the frame effect.

### 4.3 Energy dissipation capacity

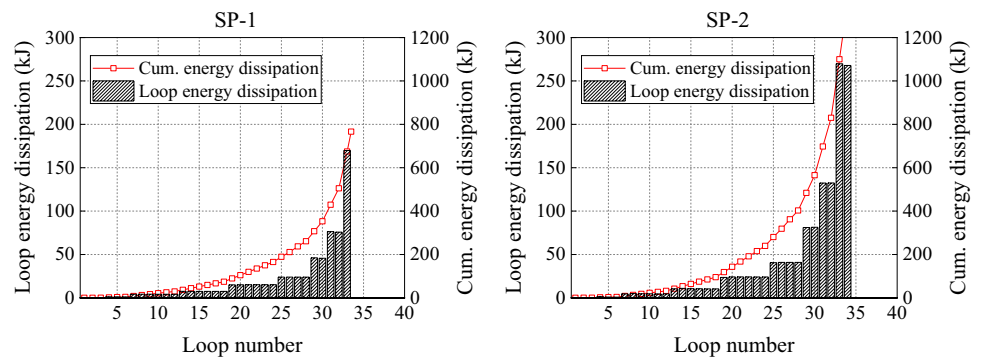
The energy dissipation capacity of a structure describes the ability of the structure to absorb seismic energy. The energy

dissipation of the specimens corresponded to the area of the hysteretic loops. The loop energy dissipation and cumulative energy dissipation of the specimens are plotted in Fig. 20. It was found that the loop and cumulated energy dissipation increased with the loading process from the initial loading stage. The specimen with higher  $\tau$  had higher energy dissipation capacity. The energy dissipations in the loading cycles with same drift ratio were almost unchanged.

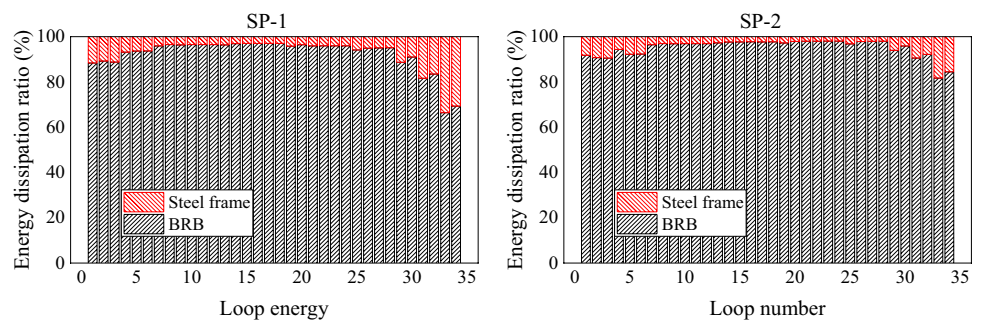
The energy dissipation ratios of the frames and BRBs are plotted in Fig. 21. It was observed that the BRB dissipated most of the seismic energy, particularly in the BRB hardening phase, where the dissipated energy of BRB were very closed to those of the overall specimen. It indicated that BRB provide enhanced energy dissipation capacity for the structure, and the inelastic deformation was limited to the BRB in the BRB hardening phase.

Table 2 lists the performance indexes of both specimens. The yield displacement ( $u_{y1}$ ) and yield force of BRBs ( $F_{y1}$ )

**Fig. 20** Cycle energy dissipation and cumulated energy dissipation of specimens



**Fig. 21** Energy dissipation ratio of specimens



**Table 2** Performance indexes of specimens

Specimen	Direction	$u_1$ (mm)	$\phi_{y1}$	$F_{y1}$ (kN)	$u_2$ (mm)	$\phi_{y2}$	$F_{y2}$ (kN)	$\mu$	$s$	R
SP-1	Positive	6.4	0.26%	522	38.4	1.5%	1098	6.0	0.48	2.9
	Negative	5.1	0.20%	406	44.0	1.8%	1219	8.6	0.33	2.9
SP-2	Positive	6.7	0.27%	811	33.8	1.4%	1463	5.0	0.55	2.8
	Negative	4.7	0.19%	672	38.6	1.5%	1538	8.2	0.44	3.6

$u_{y1}$  is yield displacement of the BRB;  $P_{y1}$  is inter-story shear corresponding to  $u_{y1}$ ;  $u_{y2}$  is yield displacement of the HSS frame;  $P_{y2}$  is inter-story shear corresponding to  $u_{y2}$ ;  $K_e$  is initial stiffness;  $\mu$  is effective displacement ductility ratio;  $s$  is overstrength factor;  $R$  is strength reduction factor

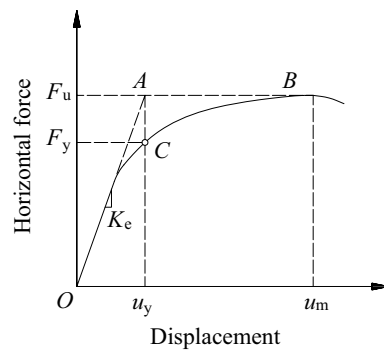


**Fig. 22** Schematic of equivalent stiffness method

were directly obtained from the hysteresis curves in Fig. 15. The yield displacement ( $u_{y2}$ ) and yield force ( $F_{y2}$ ) of the steel frames were determined based on the skeleton curves (Fig. 14) using the “equivalent initial stiffness method” [22], where the initial stiffness was obtained as the slope between the origin and the point that corresponded to 0.1 times the ultimate load (Fig. 22). The effective displacement ductility ratio was defined as  $\mu = u_{y2}/u_{y1}$ , and the overstrength factor was defined as  $s = F_{y1}/F_{y2}$ . According to the “equal displacement rule” proposed by Newmark and Hall [23], the actual reduction factor was calculated as  $R = \mu \times s$ . It was found that HSS frames exhibited large elastic deformation capacity, and the equivalent yield drift ratios for both HSS frames in both directions ranged from 1.4 to 1.8%. Accordingly, the effective ductility ratios of the two specimens in both directions ranged from 5.0 to 8.6, which indicated that the BRB developed adequate plastic deformation in the BRB hardening phase. The strength reduction factors ranged between 2.8 and 3.6, which indicated favorable capacity for reducing actions of the seismic forces.

## 5 Conclusions

An innovative dual system combined of HSS frame and BRB was studied in this paper. Two half-scaled HSSF-BRB specimens with different stiffness ratio between BRB and HSS frame were designed, fabricated and tested. The seismic performance of the HSSF-BRB specimens was evaluated based on the test results and follow-up analyses. The main conclusions of this study are summarized as follows:

1. The test observations of the HSSF-BRB specimens in the pseudo-static test can be summarized as: overall elastic deformation, yielding and hardening of the BRB, partial plastic deformation at the ends of the columns and beams, and fracture in the column base.
2. The specimens enforced an stable overall ductile mechanism in the pseudo-static test. Both specimens exhibited

favorable seismic performance, such as large deformation capacity, high elastic stiffness, significant effective ductility, excellent energy dissipation capacity and high strength reduction factor. Specimen with larger  $\tau$  had higher lateral stiffness, strength and energy dissipation capacity. The characteristics of both specimens in the pseudo-static test can be divided into three typical phases, which were described as overall elastic phase, BRB hardening phase, and failing phase.

3. The BRB hardening phase was characterized by high energy dissipation capacity, and the plastic deformation was limited to the BRB. Therefore, the ductile demand of HSS member in HSSF-BRB was reduced.
4. The horizontal force was shared by the BRB and the HSS frame. The BRB carried most of the story shear at low displacement levels, which was crucial for the flexible seismic design under frequent earthquakes.
5. High level of tensile stress appeared in the column base with large story drift, particularly for those with high  $\tau$ , resulting in fracture in the column base. Therefore, the column base should be strengthened in practical applications.
6. Despite the detailed discussion of the test results reported in this paper, finite element model will be established based on the test data in the following investigation to provide a better understanding of the seismic performance of HSSF-BRB. The major seismic parameters of HSSF-BRB (i.e. ductility, overstrength ratio, strength reduction factor and so on) will be discussed and compared with those of common BRB frames.

**Author contributions** SP: conceptualization, writing—original draft, formal analysis, data curation, validation. ZZ: supervision, funding acquisition. E-FD: conceptualization, investigation, writing—review and editing, funding acquisition, supervision. Y-BW: reviewing, supervision.

**Funding** The study was funded by the National Natural Science Foundation of China (No. 51908511), Key Research and Promotion Project (Scientific and Technological Project) of Henan Province, China (No. 212102310286), China Postdoctoral Science Foundation (No. 2019M662532) and Key Scientific Research Projects Plan of Colleges and Universities in Henan Province (No. 20A560002).

**Availability of data and materials** The datasets used or analysed during the current study are available from the corresponding author on reasonable request.

**Code availability** Not applicable.

## Declarations

**Conflict of interest** All authors certify that they have no affiliations with or involvement in any organization or entity with any financial

interest or non-financial interest in the subject matter or materials discussed in this manuscript.

## References

- Bjorhovde R. Development and use of high performance steel. *J Constr Steel Res.* 2004;60(3–5):393–400.
- IABSE. Use and application of high-performance steels for steel structures. Switzerland: IABSE, ETH Zürich; 2005.
- Haaiker G. Economy of high strength steel structural members. *J Struct Div.* 1961;87(8):1–24.
- Galambos TV, Hajjar JF, Earls CJ. Required properties of high-performance steels. NISTIR 6004. Gaithersburg: NIST. 1997
- Collin P, Johansson B. Bridges in high strength steel. In: Proceedings of IABSE symposium report, Budapest, Hungary, vol. 92; 2006. p. 1–9.
- Shi G, Hu F, Shi Y. Recent research advances of high strength steel structures and codification of design specification in China. *Int J Steel Struct.* 2014;14(4):873–87.
- Ricles JM, Sause R, Green PS. High-strength steel: implications of material and geometric characteristics on inelastic flexural behavior. *Eng Struct.* 1998;20(4/6):323–35.
- Uang CM, Bruneau M. State-of-the-art review on seismic design of steel structures. *J Struct Eng.* 2018;144(4):03118002.
- Ban HY, Shi G, Shi YJ, Wang YQ. Research Progress on the Mechanical Property of High Strength Structural Steels. *Adv Mater Res.* 2011;250–253:640–8.
- Hu FX, Shi G, Shi YJ. Experimental study on seismic behavior of high strength steel frames: Global response. *Eng Struct.* 2017;131:163–79.
- Tenchini A, D’Aniello M, Rebelo C, Landolfo R, Silva LSD, Lima L. Seismic performance of dual-steel moment resisting frames. *J Constr Steel Res.* 2014;101:437–54.
- Van Long H, Jean-François D, Lam LDP, Barbara R. Field of application of high strength steel circular tubes for steel and composite columns from an economic point of view. *J Constr Steel Res.* 2011;67(6):1001–21.
- Tenchini A, D’Aniello M, Rebelo C, Landolfo R, Da Silva LS, Lima L. High strength steel in chevron concentrically braced frames designed according to Eurocode 8. *Eng Struct.* 2016;124:167–85.
- Nakai M, Nakamura Y, Maeda S, Tanaka T, Asai H, Suzuki Y. Proposal for damage-free design method of steel structure utilizing high strength steel under great earthquake. *J Struct Construct Eng.* 2011;76(666):1443–51.
- Tian XH, Su MZ, Lian M, Wang F, Li S. Seismic behavior of K-shaped eccentrically braced frames with high-strength steel: shaking table testing and FEM analysis. *J Constr Steel Res.* 2018;143:250–63.
- Guerrero H, Escobar JA, Teran-Gilmore A. Experimental damping on frame structures equipped with buckling-restrained braces (BRBs) working within their linear-elastic response. *Soil Dyn Earthq Eng.* 2018;106:196–203.
- Deylami A, Mahdavi-pour MA. Probabilistic seismic demand assessment of residual drift for buckling-restrained braced frames as a dual system. *Struct SAF.* 2016;58:31–9.
- GB 50017–2017. Code for design of steel structures. Beijing: China Architecture & Building Press; 2017.
- GB T 22.81–2010. Metallic materials-Tensile testing-Part 1: Method of test at room temperature. Beijing: China Standards Press; 2011.
- GB 50011–2010. Code for seismic design of buildings. Beijing: China Architecture & Building Press; 2010.
- ANSI/AISC 341–10. Seismic provisions for structural steel buildings Chicago. Illinois: American Institute of Steel; 2010.
- Park R. State of the art report-ductility evaluation from laboratory and analytical testing. In: Proceedings of 9th World Conference on Earthquake Engineering. Tokyo, Japan, 1988: 605–616.
- Newmark NM, Hall WJ. Earthquake spectra and design. *Earth Syst Dyn.* 1982.

**Publisher's Note** Springer Nature remains neutral with regard to jurisdictional claims in published maps and institutional affiliations.